



HAL
open science

Small Angle X-ray Scattering analysis of porous powders of CaCO₃

Elvia Anabela Chavez Panduro, Thomas Beuvier, M. Fernandez-Martinez, Leila Hassani, Brice Calvignac, Frank Boury, Alain Gibaud

► **To cite this version:**

Elvia Anabela Chavez Panduro, Thomas Beuvier, M. Fernandez-Martinez, Leila Hassani, Brice Calvignac, et al.. Small Angle X-ray Scattering analysis of porous powders of CaCO₃. *Journal of Applied Crystallography*, 2012, 82 (3), pp.881-889. hal-03165454

HAL Id: hal-03165454

<https://univ-angers.hal.science/hal-03165454>

Submitted on 10 Mar 2021

HAL is a multi-disciplinary open access archive for the deposit and dissemination of scientific research documents, whether they are published or not. The documents may come from teaching and research institutions in France or abroad, or from public or private research centers.

L'archive ouverte pluridisciplinaire **HAL**, est destinée au dépôt et à la diffusion de documents scientifiques de niveau recherche, publiés ou non, émanant des établissements d'enseignement et de recherche français ou étrangers, des laboratoires publics ou privés.

Small-angle X-ray scattering analysis of porous powders of CaCO_3

Elvia Anabela Chavez Panduro,^a Thomas Beuvier,^a Manuel Fernández Martínez,^b Leila Hassani,^c Brice Calvignac,^c Frank Boury^c and Alain Gibaud^{a*}

^aIMMM, LUNAM, Université du Maine, Faculté de Sciences, UMR CNRS 6283, Le Mans Cedex 9, 72000, France, ^bID02, European Synchrotron Radiation Facility, Grenoble Cedex, 38043, France, and ^cLaboratoire INSERM U1066 (MINT), Bâtiment IBS – IRIS – CHU, 3ème étage, rue des Capucins, 49933 Angers Cedex 9, France. Correspondence e-mail: gibaud@univ-lemans.fr

The results of small-angle and ultra-small-angle X-ray scattering on porous CaCO_3 microparticles of pulverulent vaterite made by a conventional chemical route and by using supercritical CO_2 are presented. The scattering curves are analysed in the framework of the Guinier–Porod model, which gives the radii of gyration of the scattering objects and their fractal dimension. In addition, the porosity and the specific surface area are determined by using the Porod invariant, which is modified to take into account the effective thickness of the pellet. The results of this analysis are compared with those obtained by nitrogen adsorption.

© 2012 International Union of Crystallography
Printed in Singapore – all rights reserved

1. Introduction

Small-angle X-ray scattering (SAXS) is nowadays one of the very few techniques that can provide statistical information about the morphology, porosity and specific surface area of materials at the nanometre scale. Among the most studied materials by this technique, for which there is an abundant literature on the topic, one finds coal powders (Gibaud *et al.*, 1996; Radlinski *et al.*, 2004; Schmidt, 1982; Kalliat & Kwak, 1981). In order to extract the maximum amount of information, it is important to measure the scattering intensity in absolute units, which in turn necessitates the correction of the measured intensity for the transmission coefficient and the thickness of the material. This is one of the major problems to solve when one wants to analyse the data obtained from powders since (i) the transmitted beam intensity decays exponentially with the thickness of the sample and (ii) the real thickness can be difficult to ascertain when one is dealing with powdered samples. The analysis of the data strongly depends on how the experiment has been performed and how much effort the analyst wants to put into the model. For many years, many researchers were satisfied with standard analysis through linear plots such as Guinier or Porod plots (Guinier & Fournet, 1955; Glatter & Kratky, 1982). Nonlinear least-squares fits in which the electron density was refined were then introduced to analyse the data (Feigin & Svergun, 1987).

Guinier and Porod plots are the starting points for reaching fundamental information about the particle size (radius of gyration) and about scattering inhomogeneities through the Porod exponent, *i.e.* the slope of the scattering curve in a log–log representation. A Porod exponent of 4 points to particles with smooth surfaces, while an exponent of 3 points to very rough surfaces. An exponent of 3 can also point to scattering from ‘collapsed’ polymer chains (in a bad solvent) and an

exponent of 5/3 points to scattering from ‘fully swollen’ chains (in a good solvent). An exponent of 2 can represent scattering either from Gaussian polymer chains or from a two-dimensional structure (such as lamellae or platelets).

Although this is quite basic, there are some improvements that can be made in the way that data are analysed through this type of modelling. In particular, a paper by Beaucage & Schaefer (1994) shows how to combine the two approaches into a unified version. This approach is widely used nowadays but it was found that sometimes it yields unrealistic values for the Porod exponent. This is why Hammouda (2010) proposed to correct the Beaucage approach by imposing continuity of the scattering between the Guinier and the Porod behaviours. His model, labelled as the Guinier–Porod model, contains a constraint that is necessary to solve the problems encountered in the Porod regime found in the unified Beaucage model.

To go beyond this type of model, it is necessary to make very careful measurements of the scattering intensity, of the transmitted intensity and of the thickness of the sample. In such conditions, it is possible to obtain the porosity and the specific surface of powdered materials. Full details of the modelling were described in a very proficient way in the paper by Spalla *et al.* (2003).

In this paper, our aim is to analyse the SAXS data of meso- and macroporous spheres of CaCO_3 having the vaterite structure, as shown in Fig. 1. Vaterite exhibits a porous structure which is suitable for drug delivery (Wei *et al.*, 2008; Peng *et al.*, 2010). It is therefore important for potential applications to understand the morphology of the host matrix and to see how the synthesis affects the porosity. The samples used here are powdered samples of vaterite, which were analysed at small and ultra-small angles at the ID02 beamline of ESRF in Grenoble, France. They exhibit scattering patterns

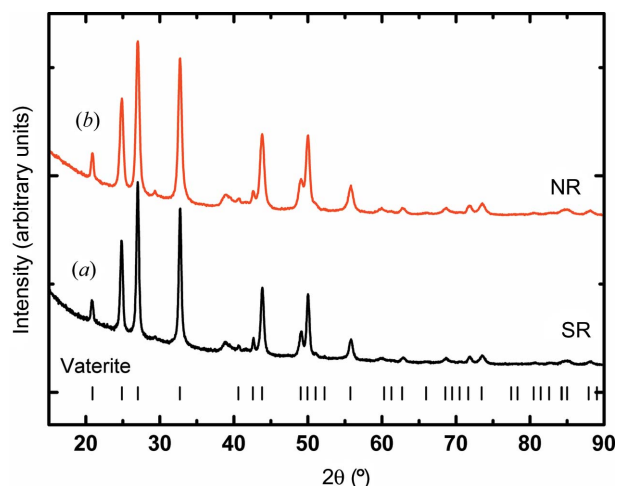


Figure 1
X-ray diffractogram of particles (a) using the high-pressure supercritical route (SR) and (b) using the normal route (NR). Bragg reflections of vaterite (ICSD 15879) are indicated by vertical markers.

arising from the hierarchical architectures observed in the microspheres of vaterite, as shown in the scanning electron microscopy (SEM) images of Fig. 2. The inner structure of the CaCO₃ microparticles can be unravelled after grinding the particles in a mortar (Beuquier *et al.*, 2011) or by cutting them by a focused ion beam (Suzuki & Hazaki, 2006). In order to access the internal structure of particles, the powder was pressed at 240 MPa and the pellet was cut into small pieces. A slide containing many broken particles was subsequently analysed by SEM. The size distributions were determined by measuring the diameters of about 200 particles. As shown in Figs. 2(a) and 2(b), the microspheres made by the normal route (NR) have an average diameter of 2.3 (10) μm. They are

composed of agglomerated nanograins. Figs. 2(c)–2(e) show the morphology of the broken particles. Radial fibrous units are observed with an important macroporosity at the cores of the particles. There is no sign of any hollow core in such particles.

Conversely, particles made by the supercritical route (SR) have a higher diameter [4.9 (10) μm; Fig. 2f]. The surface and the inner part of the particles look more compact than those of the particles made by NR (Figs. 2g and 2h). This should affect the porosity. Moreover particles made by SR have a hollow core with an average diameter of 0.7 μm (Fig. 2h). Larger particles display a larger core (Fig. 2i).

As the distribution and sizes of the macro- and mesopores in the CaCO₃ particles may differ from one particle to another, it is very difficult to model the SAXS data analytically. Therefore, we have used in this analysis the approaches of both Hammouda (2010) and Spalla *et al.* (2003) to extract real-space information contained in the scattering curves. In the SAXS analysis, we first apply the Guinier–Porod model and then we use the Porod invariant to extract the porosity and specific surface area according to the approach of Spalla *et al.* (2003).

The experimental steps in data acquisition and treatment *via* the Guinier–Porod model are described in the first part of the paper. This is done for two samples obtained by the two different synthesis routes. In the second part, we explain how the porosity and the specific surface can be measured and a comparison with BET measurements is provided.

2. Experimental

CaCO₃ powders were made by the supercritical route and the normal route. First, a solution containing 0.62 M NaCl (VWR

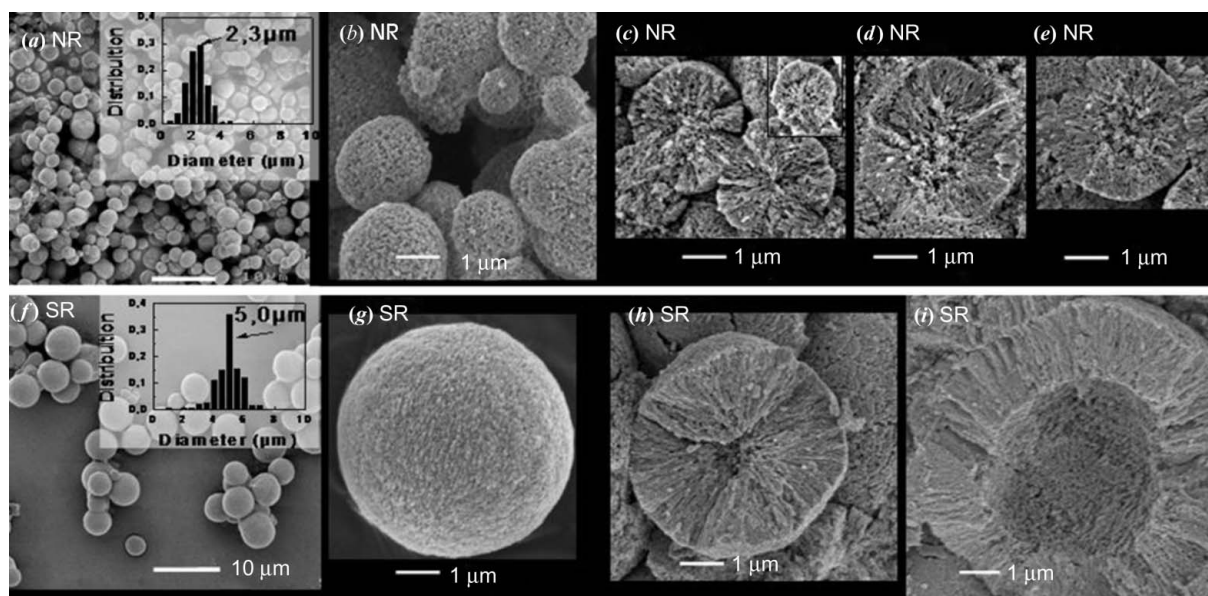


Figure 2
SEM images of CaCO₃ microparticles. (a) and (f) show that the morphology of the particles is independent of the synthesis route. The insets in these figures give the size distributions of the particles. Details about the outer structure of such particles can be observed for NR and SR in (b) and (g). Parts (c), (d) and (e) (for NR) and (h) and (i) (for SR) show cross-sectional images of the broken particles.

International, Fontenay-sous-Bois, France) and 0.62 M glycine (Sigma–Aldrich, Saint-Quentin-Fallavier, France) buffer at pH 10 was prepared. This solution is called the ‘buffer solution’. Then, calcium hydroxide Ca(OH)₂ (Sigma–Aldrich) was added [0.8% (w/v) for SR and 1.6% (w/v) for NR] to this buffer solution before adjustment of the pH to 10 and filtration (0.45 mm). Lastly, hyaluronic acid obtained from *Streptococcus equi* (Sigma–Aldrich, $M_w = 1630$ kDa) was added (0.1% w/v) to behave as a template molecule directing the polymorphism of CaCO₃ particles.

In NR, the calcic solution was mixed in equal quantity with the buffer solution containing 1.6% (w/v) of Na₂CO₃. The suspension was stirred for 5 min at 400 r min⁻¹ and at ambient temperature. The suspension of CaCO₃ microparticles was collected and centrifuged at 2400 g for 10 min. Lastly, the microparticles were washed with 50 ml of ultrapure water (Millipore, Molsheim, France), centrifuged and lyophilized (Model Lyovax GT2, Steris, Mentor, USA) to obtain a dry powder of CaCO₃.

In SR (Beuquier *et al.*, 2011), a stainless steel autoclave with a capacity of 500 ml (Separex, Champigneulle, France) was heated at 313.2 K and pressurized with CO₂ at 200 bar (20 MPa). Liquid CO₂ was pumped by a high-pressure membrane pump (Milton Roy Europe, Pont Saint Pierre, France) and preheated by a heat exchanger (Separex, Champigneulle, France) before being fed to the autoclave equipped with a mechanical stirring device (Topindustrie, Vaux le Penil, France). The axis of the magnetic stirrer was equipped with an anchor stirrer and the stirring speed was 1200 r min⁻¹. Once equilibrium was reached (temperature and pressure constant), 25 ml of aqueous solution (previously prepared) were injected by means of a high-pressure liquid chromatography pump (Model 307, Gilson, Villiers le Bel, France). The injection flow was fixed to 10 ml min⁻¹. Once addition was achieved, the final pressure was 240 bar (24 MPa) and stirring was maintained at 1200 r min⁻¹ for 5 min. Thereafter, stirring was stopped and the autoclave depressurized at a rate of 40–50 bar min⁻¹ (4–5 MPa min⁻¹). The particles were collected in the same way as for NR.

In both cases, powder was placed in a cell closed by two Kapton windows with a thickness of 50 μm separated by 1.5 mm. The powder is therefore not compressed in the cell.

SAXS and ultra-small-angle X-ray scattering (USAXS) measurements were performed at the High Brilliance beamline (ID02) at ESRF. For the SAXS experiments, a highly collimated monochromatic X-ray beam of wavelength $\lambda = 0.995$ Å passed through the pellet and the scattering intensity was recorded by an image intensified CCD-based X-ray detector (FReLoN) housed in an evacuated flight tube. The measurements were performed to a detector distance of 2 m and typical acquisition times ranged from 0.1 to 0.3 s. The measured two-dimensional SAXS patterns were normalized to an absolute scale, azimuthally averaged and background subtracted to obtain the scattering intensity $I(q)$ as a function of scattering vector $q = (4\pi/\lambda)\sin(\theta/2)$, where θ is the scattering angle. USAXS experiments were carried out in a Bonse–Hart (BH) configuration, which involves a multiple-

bounce crossed analyser. The setup provides a useful q range of $10^{-3} < q < 1$ nm⁻¹ at 12.4 keV. The instrumental background is significantly reduced using specially fabricated analyser crystals, which allowed us to measure scattering intensities down to $q \geq 0.001$ nm⁻¹. The SAXS and USAXS experiments were overlapped in order to obtain a complete scattering curve, from $q = 0.001$ to $q = 1$ nm⁻¹.

3. Theoretical aspects

3.1. The Guinier–Porod model

The elementary analysis of the data, which consisted in determining the radii of gyration and fractal dimension of the scattering objects, was carried out using the Guinier–Porod model proposed by Hammouda (2010). A more elaborate analysis, in which the porosity and the specific surface area were determined, was then performed using the approach developed by Spalla *et al.* (2003). Let us first consider the Guinier–Porod model.

It has been well known since the pioneering work of A. Guinier (Guinier & Fournet, 1955) that at very small angles of incidence, and provided that the condition $qR_g \ll 1$ is fulfilled, the SAXS intensity decreases exponentially as $\exp(-q^2R_g^2/3)$. This behaviour is generally limited to very small angles of incidence. The range of validity fundamentally depends on the radius of gyration (R_g) of the scattering particle. Beyond the Guinier regime, *i.e.* for $qR_g \gg 1$ (Porod regime), a steep decay of the scattering intensity is generally observed. This decay is found to behave as a power law of the type q^{-D_f} , in which D_f is the fractal dimension associated with the scattering objects. Beaucage proposed 20 years ago to combine these two limiting regimes into a unified equation. As pointed out in the *Introduction*, this way of analysing the data is generally quite efficient but it has the drawback of yielding overestimated values of the fractal dimension. This is why Hammouda (2010) sought to improve the model by imposing the condition that the Guinier regime be continuous with the Porod one. Hammouda (2010) used a model valid for only one type of radius of gyration. In the present paper, as we observed at least two different characteristic particle sizes in our scattering data, it was necessary to implement the Guinier–Porod model proposed by Hammouda (2010) for this specific case. The scattering intensity is thus described by the following equations:

$$\begin{aligned} I_{11} &= G_1 \exp(-q^2R_{g1}^2/3) \quad \text{for } q < q_1, \\ I_{12} &= D_1/q^{D_{f1}} \exp(-q^2R_{g2}^2/3) \quad \text{for } q > q_1, \\ I_{21} &= G_2 \exp(-q^2R_{g2}^2/3) \quad \text{for } q < q_2, \\ I_{22} &= D_2/q^{D_{f2}} \quad \text{for } q > q_2, \end{aligned} \quad (1)$$

where the Guinier and Porod terms are constrained by continuity at the positions

$$q_i = \frac{1}{R_{gi}} \left(\frac{3D_{fi}}{2} \right)^{1/2} \quad \text{with } D_i = G_i \exp\left(\frac{D_{fi}}{2}\right) \left(\frac{3D_{fi}}{2}\right)^{D_{fi}/2} R_{gi}^{-D_{fi}}, \quad (2)$$

for which $i = 1$ or 2 according to which domain one considers; G_i is a constant.

A typical scattering curve following such a model is presented in Fig. 3(a). It shows that the scattering intensity exhibits two plateaus of constant intensity followed by two steep decays, the slopes of which depend on the fractal dimension of the scattering objects. Each plateau is limited in the upward q range by a curvature of the scattering curve located at a q position defined by $q = (3D_{fi}/2)/R_g$. The linear decay observed in log–log plots, which follows the curvature, provides information about the fractal dimension of the

scattering object. In Fig. 3(a), the exponent was considered to be equal to 4, assuming smooth interfaces between the pores and the solid phase.

In this type of sample, it is easy to understand that several types of hierarchical porosities exist. The first is the macroporosity of the core (intragrain), together with the porosity existing between the grains of powder (intergrain). The second is the mesoporosity observed inside a macroparticle of vaterite (intragrain). Such porosities can be accessed by SAXS. As seen in Fig. 3(a), SAXS curves exhibit a typical shape that can be divided into two parts. The first part of the scattering curve (at small q) is due to the macropores inside and outside the microspheres, while the second one is related to the contrast of electron density between the mesopores contained in the inner structure of the microspheres. We now address how we have defined the porosity and how it can be accessed by the analysis of SAXS curves.

3.2. Determination of the porosity

In a first step, the total volume of the pellet (V_{Pellet}) is considered as the sum of the volumes occupied by the different phases, *i.e.* the macropores, the mesopores and the solid phase of vaterite:

$$V_{\text{Pellet}} = V_{\text{Macro}} + V_{\text{Meso}} + V_{\text{solid}}. \quad (3)$$

The total porosity of the pellet (Φ_P) is thus given by

$$\Phi_P = (V_{\text{Macro}} + V_{\text{Meso}})/V_{\text{Pellet}}. \quad (4)$$

Thus the system can be considered as consisting of two phases: a solid phase constituted of crystalline vaterite and a porous phase composed of mesopores (located inside the shell of the particles) and macropores found either in the core of the particles or between the particles.

For a system made of two phases, it can be shown that Porod's invariant, Q , is directly related to the porosity. The value of Q is calculated using the scattering intensity measured in absolute units (cm^{-1}):

$$Q = \int_0^\infty I_{\text{ABS}}(q) q^2 dq = 2\pi^2 \Phi_P (1 - \Phi_P) r_c^2 (\Delta\rho_e)^2, \quad (5)$$

where $I_{\text{ABS}}(q) = N/(N_0 T e_p \Delta\Omega)$ is the absolute intensity, N is the number of photons collected per second in the detector, N_0 is the number of photons in the direct beam, e_p is the thickness of the pellet, $\Delta\Omega$ is the size of a pixel seen from the sample, T is the transmission coefficient, r_c is the classical radius of the electron and $\Delta\rho_e$ is the electronic density contrast between the particles and pores. Φ_P is the total porosity of the pellet and $(1 - \Phi_P)$ is therefore the volume fraction of solid inside the pellet (Fig. 4a).

Since the invariant is calculated for $q = 0 - \infty$, it is important to understand that the total porosity Φ_P is not accessible. As measurements are limited to the range $q = 0.001 - 1 \text{ nm}^{-1}$, equation (5) gives access only to pores that are in a range inverse to the accessible q range. For the analysis, powder is therefore arranged in a double-layer conformation (see Figs. 4a and 4b): one layer contains the material and the pores visible to X-rays (which we will refer to as the 'layer visible to

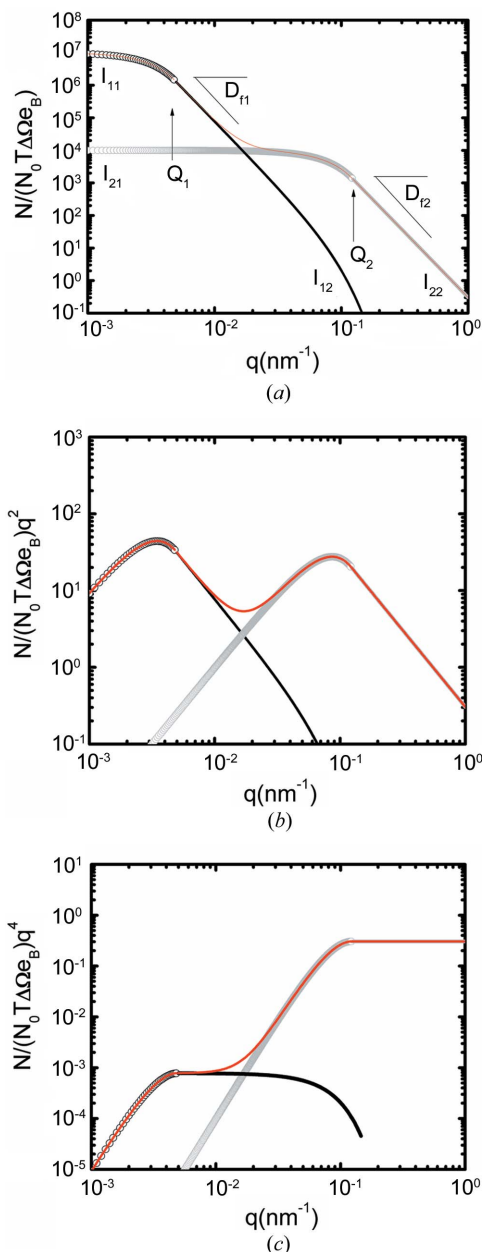


Figure 3 Typical SAXS curves calculated according to the Guinier–Porod model proposed by Hammouda (2010) for the specific case of two components. (a) $N/(N_0 T \Delta\Omega e_B)$ (cm^{-1}) versus q , where each component is characterized by a plateau followed by a steep decay having a q^{-D_i} dependence. (b) $N/(N_0 T \Delta\Omega e_B) q^2$ (cm^{-3}) versus q . (c) Porod representation $N/(N_0 T \Delta\Omega e_B) q^4$ (cm^{-5}) versus q .

X-rays'), of thickness e_V and volume V_V , and the other with a thickness $e_P - e_V$ contains only the pores not visible to X-rays.

Thus, we can express the porosity of the layer visible to X-rays as

$$\varphi^v = [V_{\text{Macro}(s < 2\mu\text{m})} + V_{\text{Meso}}]/V_V. \quad (6)$$

As a result the total porosity is given by

$$1 - \Phi_P = (V_V/V_{\text{Pellet}})(1 - \varphi^v). \quad (7)$$

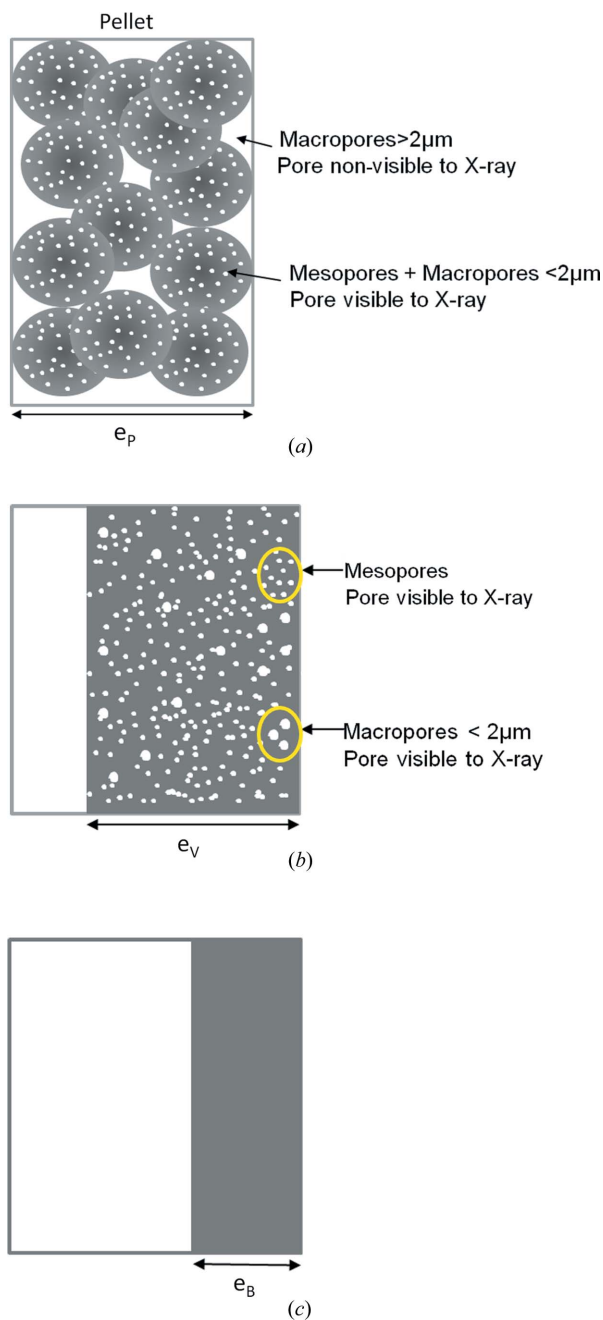


Figure 4
 (a) Representation of the pellet 'granular layer' with a thickness e_P , (b) the layer visible to X-rays with a thickness e_V and (c) the solid inside the pellet with an effective thickness e_B obtained from the transmission coefficient T .

In the expression of the invariant, the scattering that is not taken into account is that in the range $q < 0.001 \text{ nm}^{-1}$, which corresponds to the non-visible porosity. It follows that the intensity of the layer visible to X-rays is given by

$$\frac{I_V}{I_{\text{ABS}}} = \frac{e_P}{e_V} = \frac{1 - \varphi^v}{1 - \Phi_P}. \quad (8)$$

Equation (5) is directly applicable to the layer visible to X-rays by replacing the limits of integration by the accessible limits of the experiment and the porosity by the visible porosity φ^v . This yields a specific invariant denoted Q_V and defined as

$$Q_V = \int_{0.001 \text{ nm}^{-1}}^{1 \text{ nm}^{-1}} I_V(q) q^2 dq = 2\pi^2 \varphi^v (1 - \varphi^v) r_c^2 (\Delta\rho_c)^2, \quad (9)$$

where $I_V(q) = N/(N_0 T e_V \Delta\Omega)$.

As shown by Spalla *et al.* (2003) the major problem in a pulverulent material is that e_P and e_V are not known. Nevertheless, an effective thickness e_B can be obtained from the transmission coefficient T (see Fig. 4c),

$$e_B = -\ln T / \mu_{\text{solid}}, \quad (10)$$

if the absorption coefficient of the solid (μ_{solid}) is known. Considering that the pellet has a cylindrical shape with a thickness e_P , it is possible to connect the thicknesses e_P and e_B using the following relation:

$$1 - \Phi_P = e_B / e_P. \quad (11)$$

Following the work by Spalla *et al.* (2003) and equations (8) and (11) we define the intensity of the layer visible to X-rays in terms of the effective thickness (e_B) and porosity (φ^v) as follows:

$$I_V(q) = \frac{N}{N_0 T \Delta\Omega e_B} (1 - \varphi^v). \quad (12)$$

Then replacing I_V in equation (9) by equation (12), we obtain an expression in terms of measurable and known parameters,

$$\int_{0.001 \text{ nm}^{-1}}^{1 \text{ nm}^{-1}} \frac{N}{N_0 T \Delta\Omega e_B} (1 - \varphi^v) q^2 dq = 2\pi^2 \varphi^v (1 - \varphi^v) r_c^2 (\Delta\rho_c)^2, \quad (13)$$

so that the porosity can be derived as

$$\varphi^v = \frac{1}{2\pi r_c^2 (\Delta\rho_c)^2} \int_{0.001 \text{ nm}^{-1}}^{1 \text{ nm}^{-1}} \frac{N}{N_0 T \Delta\Omega e_B} q^2 dq = \frac{1}{2\pi r_c^2 (\Delta\rho_c)^2} Q_B. \quad (14)$$

The new invariant Q_B shown in equation (14) allows direct calculation of the porosity of the layer visible to X-rays, φ^v , of the pellet. Fig. 3(b) shows how the quantity $Nq^2/N_0 T \Delta\Omega e_B$ evolves as a function of q . It can be seen in such a plot that the two types of porosity give rise to two broad humps separated by a minimum. The calculation of the area between each hump and the q axis provides information about the macroporosity

Table 1

Guinier radius and fractal dimension calculated using the Guinier–Porod model.

Sample	R_{g1} (nm)	D_{f1}	R_{g2} (nm)	D_{f2}
Normal route	764	3.85	72	3.73
Supercritical route	720	4	36	3.45

(<2 μm) and the mesoporosity with the possibility to discriminate between each component.

3.3. Determination of the specific area

We now address how one can calculate the specific area associated with the macro- and mesopores found in the porous particles of vaterite. For this it is important to notice that the specific area can be calculated from the limit of the scattering intensity at high q values. For both components, the specific area can be written as

$$S_{Macro} = \frac{1}{(1 - \Phi_p)} \frac{[I_{ABS}q^4]_{[1]}}{2\pi\Delta\rho_c^2r_c^2} = \frac{1}{2\pi\Delta\rho_c^2r_c^2} \left[\frac{N}{N_0T\Delta\Omega e_B} q^4 \right]_{[1]}, \quad (15)$$

$$S_{Meso} + S_{Macro} = \frac{1}{(1 - \Phi_p)} \frac{[I_{ABS}q^4]_{[2]}}{2\pi\Delta\rho_c^2r_c^2} = \frac{1}{2\pi\Delta\rho_c^2r_c^2} \left[\frac{N}{N_0T\Delta\Omega e_B} q^4 \right]_{[2]}. \quad (16)$$

It is clear that, if the scattering intensity decays as a power law with a fractal exponent equal to 4, the plot of Iq^4 versus q will produce a straight line parallel to the q axis at high values of q . Such a behaviour is shown in Fig. 3(c), where one can see that two lines run parallel to the q axis. The lowest one is due to the surface area of the macropores (such as, for instance, the hollow core), while the upper one is related to both the macropores and the mesopores. As the macropores' contribution is known it is possible to separate the contributions of the macroscopic and mesoscopic objects.

In addition one can also foresee that the straight line parallel to the q axis will deviate from this behaviour if the fractal dimension of the object differs from 4. For objects having values of D_f smaller than 4, this plot will produce lines at high q having a positive slope.

4. Results and discussion

4.1. Application of the Guinier–Porod model

In Fig. 5, one can clearly see that the scattering curves for the NR and SR samples are in perfect agreement with the model described in the previous section. The two samples with different synthesis routes exhibit very similar scattering curves, showing that the porous structure of the two samples is somewhat similar. The differences are in the values of the radii of gyration of the two domains and in the fractal dimensions of the scattering objects. After adjustment, we observe that the $CaCO_3$ particles are composed of scattering objects with

Table 2

Calculation of the porosity and surface area of $CaCO_3$ particles from SAXS–USAXS curves using the Porod invariant and Porod plots (with integration carried out in the range $q = 0.001–1 \text{ nm}^{-1}$).

Sample	T	ϕ^v (%)	ϕ_{Macro}^v (%)	ϕ_{Meso}^v (%)	S_{Macro} ($m^2 g^{-1}$)	S_{Meso} ($m^2 g^{-1}$)
Normal route	0.42	46	24	22	1.65	16
Supercritical route	0.64	42	30	12	1.83	21

fractal dimensions close to $D_f = 4$. $D_f = 4$ indicates that the object has a smooth interface, while $3 < D_f < 4$ indicates that the object has a rough surface. The size and the fractal dimension of objects are determined from a fit to the data according to equation (1). The fitted parameters are the radii of gyration and the fractal dimensions for each domain. By supposing that the pores have a spherical shape, the real radius of the pores (R) can be deduced from the radius of gyration (R_g) by the relation (Feigin & Svergun, 1987) $R = 5/3^{1/2}R_g$. We can draw the following conclusions from the results:

(a) The first domain ($q < 0.02 \text{ nm}^{-1}$) defines the macropores of the pellet located inside and outside the microspheres. These macropores are large objects of diameter 720 nm with $D_f = 4$ for SC and diameter 764 nm with $D_f = 3.85$ for NR. These fractal dimensions are close to 4, which is consistent with the fact that the macropores have a smooth surface.

(b) The second domain ($q > 0.02 \text{ nm}^{-1}$) characterizes the presence of mesopores inside the microspheres. These mesopores are small objects of diameter 36 nm with a fractal dimension $D_f = 3.45$ for SR. For the NR sample the diameter is larger (72 nm) and the fractal dimension is $D_f = 3.73$. The fractal dimensions are less than 4, which highlights that mesopores have a rough surface (see Table 1).

It is important to note that it was possible to access this information only because SAXS and USAXS experiments were carried out. Indeed, it is impossible to probe a radius of gyration of 280 nm by conventional SAXS experiments.

4.2. Application of the Porod invariant

The effective thickness e_B of the sample was calculated using equation (10) with the transmission coefficients (T) at 12.4 keV shown in Table 2. Taking equations (10) and (11) with $\bar{e}_p = 1.5 \text{ mm}$ (see *Experimental* section), the estimated total porosity is 90 and 95% for NR and SR, respectively (these values are important because the pellets are not pressed). The electron density of vaterite was calculated from the hexagonal structure of vaterite and was found to be equal to 810 e nm^{-3} . The mass density of vaterite was taken to be 2.66 g cm^{-3} as expected from its crystalline structure, which was checked by complementary wide-angle X-ray scattering measurements. With all this information it was possible to calculate (1) the invariant $Q_B = \int N/(N_0T\Delta\Omega e_B)q^2 dq$ using the TRAPZ function in *MATLAB* (The MathWorks Inc., Natick, MA, USA), which is a built-in function for numerical integration, and (2) the porosity. The interval of integration in q space was chosen to range from 10^{-3} to 1 nm^{-1} . Since the

integration is truncated to experimental boundaries, the determination of Q_B is underestimated. At low q , a correction can be applied by assuming that the intensity is a constant. At high q , the correction can be estimated by assuming that the Porod behaviour $I(q) \simeq q^{-D_i}$ is still valid. With such assumptions, we can estimate that Q_B is reduced by about 1% at low q , while at high q the underestimation is about 20% of the value corresponding to the mesopores. The results of the porosity calculations are shown in Table 2.

The porosities calculated by the Porod invariant are $\varphi^v = 42\%$ for SR and $\varphi^v = 46\%$ for NR. It can be seen on the plots

shown in Figs. 5(c) and 5(d) that the two curves are quite similar in the low- q region, while they significantly differ at large q values. The discrimination between macro- and mesoporosities is possible from the fits to the data. Each component can be calculated by replacing the scattering intensity in the expression for Q_B by $I_1(q)$ and $I_2(q)$. The results for the meso- and macroporosities are shown in Table 2. It can be seen that the mesoporosity is much smaller for the supercritical route ($\varphi_{\text{Meso}}^v = 12\%$) than for the normal route ($\varphi_{\text{Meso}}^v = 22\%$). Note that, if we take into account the correction of Q_B at high q , the mesoporosity would be for the normal

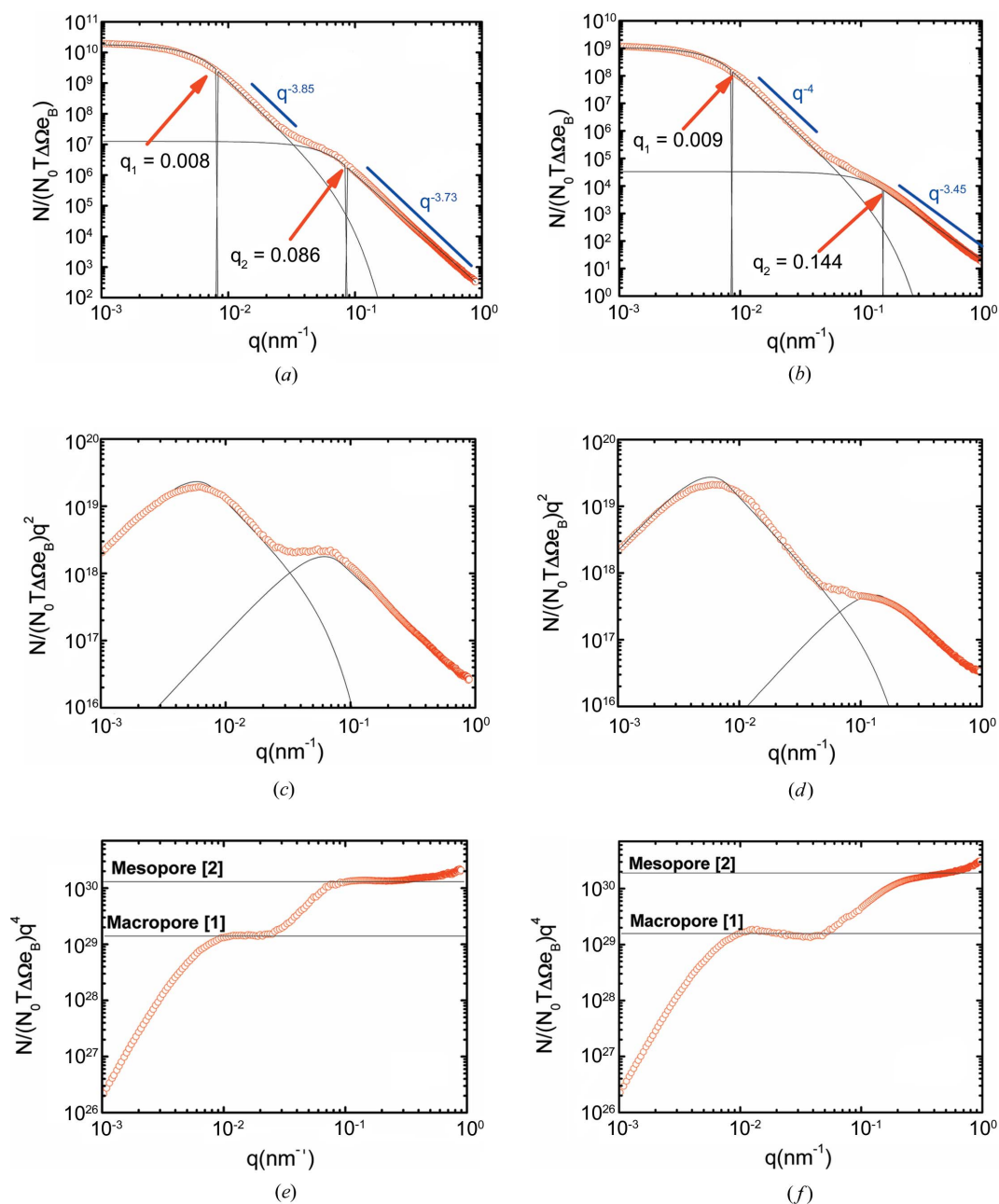


Figure 5

Experimental $N/(N_0 T \Delta \Omega e_B)$ (cm^{-1}) (circles) and calculated (with the Guinier model, solid lines) SAXS curves of CaCO_3 particles synthesised by the normal chemical route (a) and by the supercritical route (b). $N/(N_0 T \Delta \Omega e_B) q^2$ (cm^{-3}) versus q curves for the calculation of the invariant are shown in (c) and (d). Porod representations $N/(N_0 T \Delta \Omega e_B) q^4$ (cm^{-5}) versus q of the intensity of CaCO_3 particles are shown in (e) and (f).

Table 3

Comparison of porosity and surface area obtained by two methods: BJH in desorption/BET and SAXS-USAXS (with integration carried out in the range $q = 0.001\text{--}1\text{ nm}^{-1}$).

Sample	S_{Meso} ($\text{m}^2\text{ g}^{-1}$) (X-rays)	S ($\text{m}^2\text{ g}^{-1}$) (BET)	$\varphi_{\text{Meso}}^{\text{v}}$ (%) (X-rays)	φ (%) (BJH)
Normal route	16	14	22	19
Supercritical route	21	16	12	10

route $\varphi_{\text{Meso}}^{\text{v}} \approx 26\%$ and for the supercritical route $\varphi_{\text{Meso}}^{\text{v}} \approx 14\%$. On the other hand, the macroporosities are similar for the two samples, with a somewhat higher value for SR ($\varphi_{\text{Macro, SR}}^{\text{v}} = 30\% > \varphi_{\text{Macro, NR}}^{\text{v}} = 24\%$). This could be the consequence of the presence of the hollow core inside the samples prepared by SR or of the free space between the microspheres.

Figs. 5(e) and 5(f) show a plot of Iq^4 versus q . As explained in the *Theoretical Aspects* section, the two straight lines parallel to the q axis correspond to the specific surface area arising from the macropores (first plateau) and the mesopores (second plateau). Note that, since $I(q)$ is not decaying exactly as $1/q^4$, the surface area expressions in equations (15) and (16) are not correct (Wong, 1985; Bale & Schmidt, 1984). Nevertheless it is clear in Figs. 5(e) and 5(f) that the intensity times q^4 almost reaches a plateau of constant value. As the exponents do not deviate too much from 4, we considered that the

surface area could be still approximated by equations (15) and (16). The results for the specific surface area, S , are shown in Table 3. The surface area of macropores is small and quite similar for the two samples ($S_{\text{Macro}} = 1.65\text{ m}^2\text{ g}^{-1}$ for NR and $S_{\text{Macro}} = 1.83\text{ m}^2\text{ g}^{-1}$ for SR). The slightly higher value for SR may originate from the hollow core. The surface area of mesopores is much more important ($S_{\text{Meso}} = 16\text{ m}^2\text{ g}^{-1}$ for NR and $S_{\text{Meso}} = 21\text{ m}^2\text{ g}^{-1}$ for SR), with a higher value for SR mainly because of its smaller radius of gyration ($R_g = 14\text{ nm}$ for SR and $R_g = 28\text{ nm}$ for NR) and rougher surface ($D_f = 3.45$ for SR and 3.73 for NR).

To compare these results, powder samples were analysed by N_2 absorption–desorption at 77 K. The BJH (Barrett *et al.*, 1951) and BET (Brunauer *et al.*, 1938) methods were used to extract the mesoporosity and the specific surface area, respectively (Fig. 6). This technique has already been used on CaCO_3 vaterite, and several BET values have been reported [$S_{\text{BET}} = 2\text{ m}^2\text{ g}^{-1}$ (Fujiwara *et al.*, 2010), $S_{\text{BET}} = 8.8\text{ m}^2\text{ g}^{-1}$ (Volodkin *et al.*, 2004), $S_{\text{BET}} = 15.3\text{ m}^2\text{ g}^{-1}$ (Yu *et al.*, 2006), $S_{\text{BET}} = 77\text{ m}^2\text{ g}^{-1}$ (Peng *et al.*, 2010), $S_{\text{BET}} = 90\text{ m}^2\text{ g}^{-1}$ (Cai *et al.*, 2008)]. However, only a few BJH porosities have been reported. For example, Yu *et al.* (2006) obtained a mesoporosity of 16% on small hollow microspheres. Note that the analysis is restricted to pore diameters ranging between 2 and 200 nm, which in this case allows access only to mesoporosity. The results for SR and NR are shown in Table 3. The BET surface areas are $14\text{ m}^2\text{ g}^{-1}$ for NR (against $16\text{ m}^2\text{ g}^{-1}$ by SAXS analysis) and $16\text{ m}^2\text{ g}^{-1}$ for SR (against $21\text{ m}^2\text{ g}^{-1}$ by SAXS analysis). The BJH porosities obtained in desorption are 19% for NR (against 22% by SAXS) and 10% for SR (against 12% by SAXS). The agreement between these values is also quite fair and confirms that SAXS–USAXS is a convenient technique for both surface area and mesoporosity determination.

Our results show that X-ray scattering data measured by USAXS provide additional information about macroporosity that is not accessible by the BJH method. The large value of the macroporosity (24% for NR and 30% for SR) is interesting for drug encapsulation. However, we need to discriminate between the proportion of macropores inside and those outside the microspheres. Complementary investigations are presently being carried out on CaCO_3 pellets in order to see the evolution of the porosities with pressure.

5. Conclusion

We have shown in this paper that microspheres of vaterite exhibit hierarchical porosity incorporating macropores and mesopores. The quantitative determination of the pore size and of the pore smoothness was achieved by implementing the Guinier–Porod model recently proposed by Hammouda (2010) for two types of pores. The radii of gyration of the two components and their fractal dimensions were obtained. It was found that macropores have a fractal dimension close to 4, indicating smooth surfaces, whereas mesopores located inside the microspheres have a smaller fractal dimension, which highlights a rough surface. The radii of gyration are of the

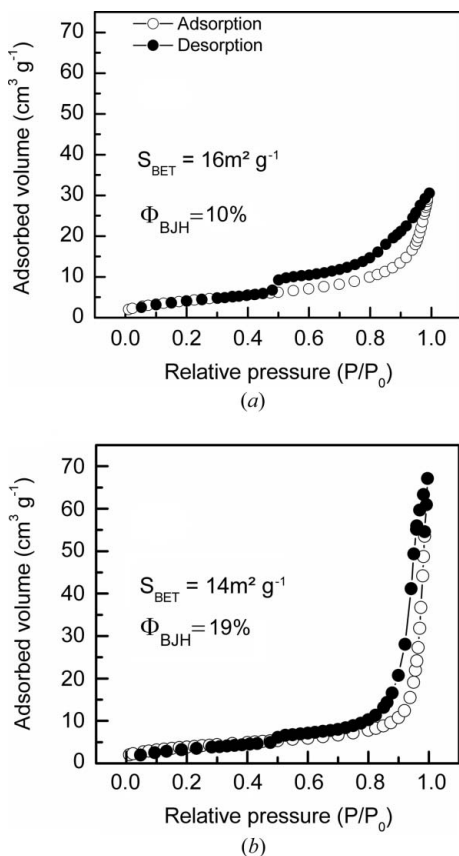


Figure 6

Nitrogen adsorption–desorption isotherms of CaCO_3 synthesized by (a) SR and (b) NR.

order of 280 nm for the macropores and about 20 times smaller for the mesopores. The porosity and the surface area were also determined following the approach of Spalla *et al.* (2003) for powders by calculating a Porod invariant based on the effective thickness of the pulverulent pellet. The specific surface and the mesoporosity are much closer to the results extracted from the N₂ adsorption–desorption analysis.

The authors are particularly grateful to ESRF for access to the ID02 beamline. They would like to thank T. Naranayan for helpful discussions. They also wish to thank the ANR for funding through the Calcomed program and the Region des Pays de la Loire and ESRF for providing financial support to EACP.

References

- Bale, H. D. & Schmidt, P. W. (1984). *Phys. Rev. Lett.* **53**, 596–599.
- Barrett, E. P., Joyner, L. G. & Halenda, P. P. (1951). *J. Am. Chem. Soc.* **73**, 373–380.
- Beaucage, G. & Schaefer, D. W. (1994). *J. Non-Cryst. Solids*, **172–174**, 797–805.
- Beuvier, T., Calvignac, B., Delcroix, J. R., Tram, M. K., Kodjikian, S., Delorme, N., Bardeau, J. F., Gibaud, A. & Boury, F. (2011). *J. Mater. Chem.* **21**, 9757–9761.
- Brunauer, S., Emmett, P. H. & Teller, E. (1938). *J. Am. Chem. Soc.* **60**, 309–319.
- Cai, A., Xu, X., Pan, H., Tao, J., Liu, R., Tang, R. & Cho, K. (2008). *J. Phys. Chem.* **112**, 11324–11330.
- Feigin, L. A. & Svergun, D. I. (1987). *Structure Analysis by Small-Angle X-ray and Neutron Scattering*, edited by George W. Taylor. New York, London: Plenum Press.
- Fujiwara, M., Shiokawa, K., Araki, M., Ashitaka, N., Morigaki, K., Kubota, T. & Nakahara, Y. (2010). *Cryst. Growth Des.* **10**, 4030–4037.
- Gibaud, A., Xue, J. S. & Dahn, J. R. (1996). *Carbon*, **34**, 499.
- Glatter, O. & Kratky, O. (1982). *Small Angle X-ray Scattering*. London: Academic Press.
- Guinier, A. & Fournet, G. (1955). *Small Angle Scattering of X-rays*. New York: Wiley.
- Hammouda, B. (2010). *J. Appl. Cryst.* **43**, 716–719.
- Kalliat, M., Kwak, C. Y. & Schmidt, P. W. (1981). *New Approaches in Coal Chemistry*, edited by B. D. Blaustein, B. C. Bockrath & S. Friedman, American Chemical Society Symposium Series Vol. 169, p. 3. Washington, DC: American Chemical Society.
- Peng, C., Zhao, Q. & Gao, C. (2010). *Colloids Surf. A Physicochem. Eng. Asp.* **353**, 132–139.
- Radlinski, A. P., Mastalerz, M., Hinde, A. L., Hainbuchner, M., Rauch, H., Baron, M., Lin, J. S., Fan, L. & Thiyagarajan, P. (2004). *Int. J. Coal Geol.* **59**, 245–271.
- Schmidt, P. W. (1982). *J. Appl. Cryst.* **15**, 567–569.
- Spalla, O., Lyonard, S. & Testard, F. (2003). *J. Appl. Cryst.* **36**, 338–347.
- Suzuki, W. & Hazaki, E. (2006). US Patent 7 015 483.
- Volodkin, D. V., Larionova, N. I. & Sukhorukov, G. B. (2004). *Biomacromolecules*, **5**, 1962–1972.
- Wei, W., Ma, G. H., Hu, G., Yu, D., McLeish, T., Su, Z. G. & Shen, Z. Y. (2008). *J. Am. Chem. Soc.* **130**, 15808–15810.
- Wong, P. Z. (1985). *Phys. Rev. B*, **32**, 7417–7424.
- Yu, J., Guo, H., Davis, S. A. & Mann, S. (2006). *Adv. Funct. Mater.* **16**, 2035–2041.